Engineering with Computers
https://doi.org/10.1007/s00366-022-01670-1

ORIGINAL ARTICLE

Effect of moisture on the nonlinear viscoelastic fracture behavior of polymer nanocompsites: a finite deformation phase-field model

Behrouz Arash[1] · **Wibke Exner**[2] · **Raimund Rolfes**[1]

Received: 13 January 2022 / Accepted: 28 April 2022

Abstract

The mechanisms underlying damage in high-performance polymer nanocomposites are remarkably affected by hygrothermal conditions. In this study, we develop a phase-field formulation to investigate the influence of hygrothermal conditions on the nonlinear viscoelastic fracture behavior of epoxy resins and their nanocomposites at finite deformation. For this, the Helmholtz free energy, capturing the effect of temperature and moisture and nanoparticle contents, is defined based on an additive decomposition of the energy into an equilibrium, a non-equilibrium, and a volumetric contribution with different definitions under tensile and compressive loading. The coupled displacement phase-field problem is solved using a quasi-Newton monolithic algorithm and a staggered solution scheme. Numerical examples show that the monolithic algorithm is more efficient. Simulations are performed to investigate the effect of temperature, deformation rate, and moisture content on the force–displacement response of boehmite nanoparticle/epoxy samples in benchmark numerical problems. Comparing numerical predictions and experimental data for compact-tension tests shows good agreement at different nanoparticle contents. Also, the model's capability to predict fracture patterns is evaluated using simulations of single-edge notched nanocomposite plates under tensile and shear loading.

Keywords Nanocomposite · Nonlinear viscoelasticity · Phase-field modeling · Finite element · Finite deformation

List of symbols

$\boldsymbol{F}, \bar{\boldsymbol{F}}$	The total deformation gradient and its deviatoric part
$\bar{\boldsymbol{F}}_e, \bar{\boldsymbol{F}}_i$	Elastic and inelastic parts of $\bar{\boldsymbol{F}}$
$\bar{\boldsymbol{B}}, \bar{\boldsymbol{B}}_e$	The total and elastic left Cauchy–Green deformation tensors
J	The volume variation
J_m, J_Θ, J_w	The mechanical compressibility, thermal dilatation and moisture-induced swelling
α_w, α_Θ	The thermal expansion and moisture swelling coefficients
Θ	Absolute temperature
v_{np}, w_w	BNP volume and moisture weight fractions
a_w, b_w	Parameters to define the effect of moisture
$\boldsymbol{\sigma}$	The Cauchy stress
$\boldsymbol{D}$	The symmetric Eulerian rate of the deformation tensor
$\boldsymbol{L}$	The Eulerian gradient of velocity
ψ	The Helmholtz free specific energy
$\psi^{\pm}$	Positive/negative parts of the free specific energy
$\psi_{eq}, \psi_{neq}, \psi_{vol}$	Equilibrium, non-equilibrium, and volumetric parts of the free specific energy
ϕ	The phase-field parameter
$g(\phi)$	The energetic degradation function
$\bar{\boldsymbol{V}}_e, \bar{\boldsymbol{R}}_e$	The pure deformation and rotation obtained from the polar decomposition of $\bar{\boldsymbol{F}}_e$
$\bar{\boldsymbol{D}}_i, \bar{\boldsymbol{W}}_i$	The rate of stretching and spin
$\bar{\boldsymbol{D}}_i^{\mathring{0}}$	The objective rate of inelastic deformation

✉ Behrouz Arash
b.arash@isd.uni-hannover.de

[1] Present Address: Institute of Structural Analysis, Leibniz Universität Hannover, Appelstraße 9A, 30167 Hannover, Germany

[2] Institute of Composite Structures and Adaptive Systems, DLR (German Aerospace Center), Lilienthalplatz 7, 38108 Brunswick, Germany

Published online: 23 May 2022

$\bar{\boldsymbol{L}}_i$	The velocity gradient of the relaxed configuration
$\boldsymbol{\sigma}_{eq}, \boldsymbol{\sigma}_{neq}$	Equilibrium and non-equilibrium stresses
$\boldsymbol{\sigma}_{dev}, \boldsymbol{\sigma}_{vol}$	Deviatoric and volumetric parts of stress
$\dot{\varepsilon}_i$	The viscoelastic flow
$\dot{\varepsilon}_i, \Delta H, \tau_0$	A pre-exponential factor, the activation energy, and the athermal yield stress
$I_1(.)$	The first invariant of a tensor
X	A modified amplification factor
μ_{eq}, μ_{neq}, k_v	Material parameters
∇	The gradient operator
$\boldsymbol{n}$	The outward unit normal
$\boldsymbol{b}, \boldsymbol{t}$	The body force and boundary tractions
G_c	The energy release rate
l_0	The length scale
$\mathcal{H}$	The local history field
$\boldsymbol{u}$	The displacement field
$\mathbf{w}_u, w_\phi$	The weight functions
$\boldsymbol{N}_u, \boldsymbol{N}_\phi$	The shape function matrices
$\boldsymbol{B}_u, \boldsymbol{B}_\phi$	The gradient operators
$\boldsymbol{K}_i^{uu}, \boldsymbol{K}_i^{u\phi}, \boldsymbol{K}_i^{\phi u}, \boldsymbol{K}_i^{\phi\phi}$	The tangent matrices
$\widetilde{\boldsymbol{K}}$	The approximated stiffness matrix
$\mathbb{C}^{\sigma J}$	The tangent modulus tensor
$\hat{\boldsymbol{F}}$	Perturbed deformation gradient
ϵ	A small perturbation parameter

1 Introduction

One of the main challenges in today's engineering is structural weight reduction to provide higher performance and functionality for specific applications. Therefore, besides structural optimization, research is also focused on developing new materials with enhanced thermo-mechanical properties at low weight. One of these new classes of materials is polymer nanocomposites, where the functionalities of polymers, including low weight and high ductility, are combined with the nanoparticles' unique features [37, 57]. Recently, boehmite nanoparticle (BNP) reinforced epoxy composites have been considered as one of the most promising composites in lightweight structures due to their high strength-to-weight ratio [31]. BNP/epoxy nanocomposites exhibit remarkably improved mechanical properties, including strength and fracture toughness, compared with neat epoxies [7, 31].

The material innovation demands reliable models to predict the effect of external conditions (e.g., loading rate, temperature, and moisture) and microstructural parameters (e.g., nanoparticle/matrix interactions) on the damage and fracture behavior of the nanocomposites. Continuing research activity on polymers and their composites has led to a variety of phenomenological or physically motivated constitutive models [48, 50] to elucidate their nonlinear rate- and temperature-dependent behavior. Boyce et al. [12] developed a constitutive model based on a composite-type formulation considering the microstructure of semicrystalline polymers. In the model, the soft amorphous and stiff crystalline phases are treated as the matrix and fillers, respectively. Later, based on the model, Qi and Boyce [53] proposed a viscoelastic–viscoplastic constitutive model to capture the nonlinear, rate-dependent, and softening behavior of thermoplastic polyurethanes. Li et al. [36] introduced a physically based viscoelastic constitutive model for elastomers at large deformation, where elastomers are assumed to be cross-linked networks with superimposed free chains. Nguyen et al. [48] developed and experimentally calibrated a rate-dependent damage constitutive model for epoxy resins to study the nonlinear behavior of amorphous glassy polymers. Based on the definition of Helmholtz free energy, N'Guyen et al. [49] derived a thermodynamical framework for the thermo-chemo-mechanical couplings in polymer materials at finite deformation. Predicting the nonlinear stress–strain response of polymer nanocomposites, which also contain nano-scale additives, is more challenging due to the heterogeneous distribution of agglomerated nanoparticles in the matrix and complex interactions between the matrix and nanoparticles. Fankhänel et al. [20] presented an atomistically informed finite-element (FE) model to study the material properties of BNP/epoxy nanocomposites. Within the multiscale model, the interphase properties between BNPs and an epoxy matrix were first characterized using molecular simulations. The interphase properties were then upscaled to the continuum scale, where the effective material properties were homogenized using FE simulations of representative volume elements of the nanocomposite. Arash et al. [6, 7] proposed a combined simulation-experiment framework to calibrate a viscoelastic damage model for BNP/epoxy nanocomposites at finite deformation. The experimental-numerical validation proves the predictive capability of the model to capture the main features of the stress–strain relationship of the nanocomposites, including the nonlinear hyperelastic, rate-dependent, and softening behavior. The experimental-numerical validation proves the capability of the model to capture the main features of the stress-strain relationship of the nanocomposites, including the nonlinear hyperelastic, rate-dependent, and softening behavior. In seeking a robust parameter identification procedure, Unger et al. [59, 60] extended the multiscale approach to characterize the thermo-viscoelastic damage behavior of BNP/epoxy nanocomposites. These studies show that the proposed simulation-based framework allows significantly reducing the

number of experimental tests required for identifying the material parameters used in modeling polymer nanocomposites without significant loss in accuracy.

As explained in [15, 48], the evolution of damage in polymer materials at the small scales, such as microvoids and microcracks coalesce, leads to the birth of cracks at the macro-scale. The progressive evolution of damage tends to the localization of deformation into a narrow zone accompanied by a softening behavior. Therefore, the modeling of fracture in nanocomposites requires an accurate prediction of damage initiation and propagation in the materials. However, FE models based on local continuum description of damage [6, 7] suffer from an inherent mesh dependence for strain softening problems [22, 47], resulting from ill-posedness of the boundary value problem due to the loss of ellipticity in statics or hyperbolicity in dynamics. To ensure the well-posedness of the boundary value problems, various computational techniques have been proposed in the literature. The so-called regularized solutions for damage and failure in materials, allowing interactions between neighboring material points, are among the most successful. The solutions link the continuum damage mechanics to fracture mechanics through the coupling of a diffusion-type equation of nonlocal variables with the momentum balance equation. A nonlocal variable, such as damage, is related to the spatial average of the field of the variable in a certain neighborhood of a given point [9]. In these methods, such as the gradient-enhanced damage model and its variants [8, 51, 52, 61], and the phase-field model (PFM) [3, 21, 44], a sharp crack is approximated by a diffuse damage band thanks to introducing a length-scale parameter that controls interactions between material points.

Generalizing Griffith's theory, PFMs have emerged as variational fracture models to adequately predict the crack initiation, propagation, and branching [1, 2, 54, 65, 67]. In these models, a fracture can be revisited as the minimization of the potential energy consisting of the stored bulk energy, the work of external forces, and the surface energy. In addition, an auxiliary variable, the so-called phase-field parameter, describes a smooth transition from an intact material to a fully broken state. PFMs have been used to study brittle fracture [11, 43], quasi-brittle fracture [19, 63], and ductile fracture [1, 42]. Among others, Msekh et al. [45, 46] developed PFMs for clay/epoxy nanocomposites, where clay nanoparticles were modeled as linear elastic materials embedded in a hyperelastic matrix. The models were also used to investigate the surface energy dissipation in the nanocomposites during fracture. Recently, Goswami et al. [25, 26] proposed a neural network algorithm for phase-field modeling fracture in brittle materials by minimizing the variational energy of a system. The simulation results show that the crack path predicted by the proposed approach is in agreement with those reported in the literature. Furthermore, some PFMs have been developed to study the rate-dependent fracture of solids [14, 38, 55, 65]. Shen et al. [55] derived phase-field formulations for fracture of viscoelastic materials at small deformation. Loew et al. [38] calibrated a rate-dependent PFM for rubbers, where the material parameters were extracted using uniaxial tensile and double-edge tensile tests. Moreover, digital image correlation determined the length-scale parameter by measuring local strain at the crack tip. Yin and Kaliske [65] integrated a viscoelastic model into a PFM to study the rate-dependent fracture behavior of elastomers. In this model, different from those proposed in [55] and [65], the crack driving force does not include the viscous energy dissipation. Instead, the driving force is defined by the elastic strain potential given by the equilibrium and non-equilibrium networks of the viscoelastic model. Brighenti [14] proposed a PFM for elastomers using a statistical physics-based micromechanical model, which captures the rearrangement of a polymer network over time. Due to the non-convexity of the total potential energy functional with respect to the kinematic variables in PFMs, hindering convergence and robustness in Newton method-based monolithic methods, different numerical strategies have been suggested to overcome the drawback [18, 23, 28, 40, 56]. Among them, staggered solution schemes [11, 43] have been shown to be robust to solve the coupled damage-displacement governing equations, but they offer computationally expensive solutions.. Recently, to remedy the computational overheads, a quasi-Newton method-based monolithic algorithm has been proposed in [34, 64] as a robust and numerically efficient solution scheme for phase-field fracture modeling.

As for thermoset nanocomposites, nanoparticle–polymer matrix interactions and ambient conditions (e.g., temperature and moisture) affect the evolution of damage [17, 30, 60]. In this contribution, to address the open questions, we derive a phase-field formulation for investigating the effect of hygrothermal conditions on the rate-dependent fracture behavior of BNP/epoxy nanocomposites at finite deformation. The corresponding free specific energy is defined on the basis of a volumetric-deviatoric decomposition of the total deformation gradient, where the volumetric part is split into positive/negative components. Modified Guth–Gold and Kitagawa models are adopted to study the influence of the nanoparticle and moisture contents and temperature on the crack propagation in the polymer nanocomposites. The coupled governing equations are solved using a quasi-Newton monolithic algorithm and a staggered solution scheme. Numerical examples confirm that the monolithic algorithm yields identical results to the staggered solution with higher efficiency. The effect of temperature, deformation rate, and moisture content on the force–displacement behavior of the nanocomposite samples are studied using the numerical simulation of benchmark problems. Also, the proposed model is

validated through the comparison of numerical predictions obtained from the modeling of compact-tension (CT) tests with experimental data.

This work is organized as follows. Sect. 2 presents a nonlinear viscoelastic model describing the temperature- and moisture-dependent behavior of polymer nanocomposites at finite deformation. The governing equations of the PFM and the corresponding discretized equations are provided in Sect. 3. In Sect. 4, the proposed PFM is validated using the numerical simulations, and the effect of temperature, deformation rate, and moisture on the fracture behavior of the nanocomposites is investigated. Finally, Sect. 5 summarizes the findings.

2 Constitutive model for nanoparticle/epoxy

The stress response of a nanoparticle/epoxy system shown in Fig. 1 can be decomposed into an equilibrium part and a viscous part to capture the nonlinear and rate-dependent behavior of the material at finite deformation [7]. In the following section, a constitutive law, which models the nanocomposites as homogeneous continua by neglecting complex interactions between nanoparticles and the epoxy matrix, is presented. The approach is suitable for modeling the nanocomposites at the macro-scale.

2.1 Kinematics

The total deformation gradient $\mathbf{F}$ is multiplicatively split into a volumetric and a deviatoric part to define the kinematics as [49]

$$\boldsymbol{F} = J^{1/3}\bar{\boldsymbol{F}}, \tag{1}$$

where $J = \det[\boldsymbol{F}]$ and $\bar{\boldsymbol{F}}$ are the volume variation and the isochoric deformation gradient, respectively. Here, it is assumed that the volume variation can be decomposed into three terms: the mechanical compressibility J_m, the thermal dilatation J_Θ, and the moisture-induced swelling J_w

$$J = J_m J_\Theta J_w, \tag{2}$$

where

$$J_\Theta = 1 + \alpha_\Theta\left(\Theta - \Theta_0\right), \tag{3}$$

and

$$J_w = 1 + \alpha_w w_w. \tag{4}$$

The proposed form for J_w to define the swelling is based on the simulation results presented in [16]. In the above equations, α_Θ and α_w are, respectively, the thermal expansion and moisture swelling coefficients, Θ is the absolute temperature, Θ_0 is the temperature of the reference configuration, and w_w is the moisture content. The deviatoric part of the deformation gradient can also be decomposed into elastic and inelastic parts by introducing an intermediate configuration as follows [35]:

$$\bar{\boldsymbol{F}} = \bar{\boldsymbol{F}}_e\bar{\boldsymbol{F}}_i. \tag{5}$$

Accordingly, the total and elastic left Cauchy–Green deformation tensors, related to the reference configuration, are given by

$$\bar{\boldsymbol{B}} = \bar{\boldsymbol{F}}\bar{\boldsymbol{F}}^T, \tag{6}$$

and

$$\bar{\boldsymbol{B}}_e = \bar{\boldsymbol{F}}_e\bar{\boldsymbol{F}}_e^{\,T}. \tag{7}$$

2.2 Clausius–Duhem inequality

To derive the constitutive law coupled to the phase-field evolution within the kinematic framework, we proceed with the Clausius–Duhem inequality for an isothermal process. Combining the first and second principles of thermodynamics, the inequality in an Eulerian configuration reads

$$\mathcal{D} = \boldsymbol{\sigma} : \boldsymbol{D} - \rho\dot{\psi} \geq 0. \tag{8}$$

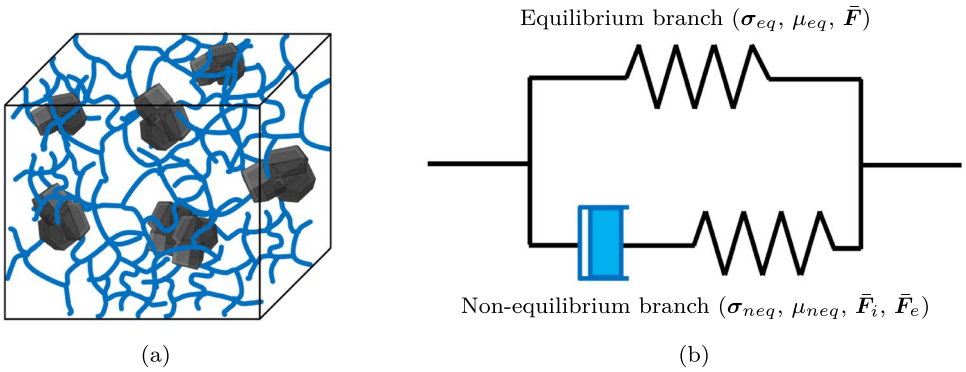

Fig. 1 **a** Micro-scale structure BNPs (gray particles) embedded in a epoxy matrix (blue chains). **b** Schematic of the viscoelastic constitutive model

Here, $\mathcal{D}$ is the dissipation, $\boldsymbol{\sigma}$ is the Cauchy stress, $\boldsymbol{D} = \frac{1}{2}\left(\boldsymbol{L} + \boldsymbol{L}^T\right)$ the symmetric Eulerian rate of the deformation tensor, and $\dot{\psi}$ is the material time derivative of the Helmholtz free specific energy. $\boldsymbol{L} = \dot{\boldsymbol{F}}.\boldsymbol{F}^{-1}$ represents the Eulerian gradient of velocity. The Helmholtz free specific energy is defined by

$$\psi = \psi\left(\bar{\boldsymbol{B}}, \bar{\boldsymbol{B}}_e, J, \phi\right), \tag{9}$$

where cracks are characterized by a phase-field parameter ϕ varying between 0 and 1. $\phi = 0$ denotes an intact material and $\phi = 1$ represents a fully cracked material. The material time derivative of the free energy is then given by [8]

$$\dot{\psi} = \frac{\partial \psi}{\partial \bar{\boldsymbol{B}}} : \dot{\bar{\boldsymbol{B}}} + \frac{\partial \psi}{\partial \bar{\boldsymbol{B}}_e} : \dot{\bar{\boldsymbol{B}}}_e + \frac{\partial \psi}{\partial J}\dot{J} + \frac{\partial \psi}{\partial \phi}\dot{\phi}, \tag{10}$$

where

$$\dot{\bar{\boldsymbol{B}}} = \boldsymbol{L}\bar{\boldsymbol{B}} + \bar{\boldsymbol{B}}\boldsymbol{L}^T - \frac{2}{3}(\boldsymbol{1} : \boldsymbol{D})\bar{\boldsymbol{B}}, \tag{11}$$

$$\begin{aligned}\dot{\bar{\boldsymbol{B}}}_e = {} & \boldsymbol{L}.\bar{\boldsymbol{B}}_e + \bar{\boldsymbol{B}}_e\boldsymbol{L}^T - 2\bar{\boldsymbol{V}}_e\bar{\boldsymbol{D}}_i^0\bar{\boldsymbol{V}}_e \\ & - \frac{2}{3}(\boldsymbol{1} : \boldsymbol{D})\bar{\boldsymbol{B}}_e, \text{and}\end{aligned} \tag{12}$$

$$\dot{J} = J(\boldsymbol{1} : \boldsymbol{D}). \tag{13}$$

The pure deformation $\bar{\boldsymbol{V}}_e$ in Eqs. (11) and (12) is obtained from the polar decomposition of $\bar{\boldsymbol{F}}_e = \bar{\boldsymbol{V}}_e.\bar{\boldsymbol{R}}_e$, and the objective rate of inelastic deformation $\bar{\boldsymbol{D}}_i^0$ is given by

$$\bar{\boldsymbol{D}}_i^0 = \bar{\boldsymbol{R}}_e\bar{\boldsymbol{D}}_i\bar{\boldsymbol{R}}_e^T, \tag{14}$$

where

$$\bar{\boldsymbol{D}}_i = \frac{1}{2}\left(\bar{\boldsymbol{L}}_i + \bar{\boldsymbol{L}}_i^T\right) = \left(\dot{\bar{\boldsymbol{F}}}_i.\bar{\boldsymbol{F}}_i^{-1}\right)_{sym}. \tag{15}$$

The velocity gradient of the relaxed configuration $\bar{\boldsymbol{L}}_i$ can be additively decomposed into a symmetric tensor $\bar{\boldsymbol{D}}_i$ and a skew-symmetric tensor $\bar{\boldsymbol{W}}_i$, so-called the rate of stretching and spin, respectively, such that $\bar{\boldsymbol{L}}_i = \bar{\boldsymbol{D}}_i + \bar{\boldsymbol{W}}_i$. Since the intermediate configuration can be taken in different ways, a convenient form for the spin of the relaxed state without loss of generality is $\bar{\boldsymbol{W}}_i = \boldsymbol{0}$ [10, 13]. By substituting Eqs. (11)-(13) into Eq. (10), we arrive at

$$\begin{aligned}\dot{\psi} = {} & \left(2\bar{\boldsymbol{B}}\frac{\partial \psi}{\partial \bar{\boldsymbol{B}}} + 2\bar{\boldsymbol{B}}_e\frac{\partial \psi}{\partial \bar{\boldsymbol{B}}_e} + J\frac{\partial \psi}{\partial J}\boldsymbol{1}\right) : \boldsymbol{D} \\ & - \frac{2}{3}(\boldsymbol{1} : \boldsymbol{D})\left(\bar{\boldsymbol{B}} : \frac{\partial \psi}{\partial \bar{\boldsymbol{B}}} + \bar{\boldsymbol{B}} : \frac{\partial \psi}{\partial \bar{\boldsymbol{B}}_e}\right) \\ & - 2\left(\bar{\boldsymbol{V}}_e\frac{\partial \psi}{\partial \bar{\boldsymbol{B}}_e}\bar{\boldsymbol{V}}_e\right) : \bar{\boldsymbol{D}}_i^0 \\ & + \frac{\partial \psi}{\partial \phi}\dot{\phi}.\end{aligned} \tag{16}$$

Finally, introducing relation (16) into (8), we obtained the dissipation inequality

$$\begin{aligned}& \underbrace{\left(\boldsymbol{\sigma} - 2\rho\left(\bar{\boldsymbol{B}}\frac{\partial \psi}{\partial \bar{\boldsymbol{B}}} + \bar{\boldsymbol{B}}_e\frac{\partial \psi}{\partial \bar{\boldsymbol{B}}_e}\right)^D - J\frac{\partial \psi}{\partial J}\boldsymbol{1}\right) : \boldsymbol{D} + 2\rho\left(\bar{\boldsymbol{B}}_e\frac{\partial \psi}{\partial \bar{\boldsymbol{B}}_e}\right)^D : \bar{\boldsymbol{D}}_i^0}_{\mathcal{D}_m} \\ & + \underbrace{\left(-\rho\frac{\partial \psi}{\partial \phi}\dot{\phi}\right)}_{\mathcal{D}_\phi} \geq 0.\end{aligned} \tag{17}$$

To proceed further, we make two assumptions based on Germain's work [24]: $\mathcal{D}_m$ and $\mathcal{D}_\phi$ are independently positive, and the dissipation results from the thermodynamic flux or force related to the internal variable $\bar{\boldsymbol{F}}_i$. Based on the assumptions, the thermodynamic force related to the flux $\boldsymbol{D}$ has to remain null regardless of the thermodynamic process. Therefore, the the stress can be split into equilibrium $\boldsymbol{\sigma}_{eq}$, non-equilibrium $\boldsymbol{\sigma}_{neq}$, and volumetric $\boldsymbol{\sigma}_{vol}$ terms as follows:

$$\boldsymbol{\sigma} = \underbrace{2\rho\left(\bar{\boldsymbol{B}}\frac{\partial \psi}{\partial \bar{\boldsymbol{B}}}\right)^D}_{\boldsymbol{\sigma}_{eq}} + \underbrace{2\rho\left(\bar{\boldsymbol{B}}_e\frac{\partial \psi}{\partial \bar{\boldsymbol{B}}_e}\right)^D}_{\boldsymbol{\sigma}_{neq}} + \underbrace{J\frac{\partial \psi}{\partial J}\boldsymbol{1}}_{\boldsymbol{\sigma}_{vol}}, \tag{18}$$

where superscript D denotes the deviatoric operator. The following terms remain in the dissipation:

$$\underbrace{2\rho\left(\bar{\boldsymbol{B}}_e\frac{\partial \psi}{\partial \bar{\boldsymbol{B}}_e}\right)^D}_{\boldsymbol{\sigma}_{neq}} : \quad \bar{\boldsymbol{D}}_i^0 - \rho\frac{\partial \psi}{\partial \phi}\dot{\phi} \geq 0. \tag{19}$$

Assuming that two terms in Eq. (19) are independently positive, $\bar{\boldsymbol{D}}_i^0$ is therefore

$$\bar{\boldsymbol{D}}_i^0 = \frac{\dot{\epsilon}_i}{\tau_{neq}}\boldsymbol{\sigma}_{neq}, \tag{20}$$

where $\tau_{neq} = \left\|\boldsymbol{\sigma}_{neq}\right\|_F$. Equation (20) is a natural choice for $\bar{\boldsymbol{D}}_i^0$ to make the first term of Eq. (19) a positive-definite quadratic form. Using Eq. (14), it can be remarked that

$$\bar{\boldsymbol{D}}_i = \frac{\dot{\varepsilon}_i}{\tau_{neq}} \bar{\boldsymbol{R}}_e^{\,T} \boldsymbol{\sigma}_{neq} \bar{\boldsymbol{R}}_e, \tag{21}$$

and the viscoelastic flow $\dot{\varepsilon}_i$ is defined by the Argon model [62]

$$\dot{\varepsilon}_i = \dot{\varepsilon}_0 \exp\left[\frac{\Delta H}{k_b \Theta}\left(\left(\frac{\tau_{neq}}{\tau_0}\right)^{5/6} - 1\right)\right], \tag{22}$$

where k_b is the Boltzmann constant. The model is characterized by a pre-exponential factor $\dot{\varepsilon}_0$, the activation energy ΔH, and the athermal yield stress τ_0. Recently, Unger et al. [60] showed that the Argon model leads to a good agreement with experimental data in a wide range of temperatures. Substituting Eq. (21) into Eq. (15) gives

$$\dot{\bar{\boldsymbol{F}}}_i = \frac{\dot{\varepsilon}_i}{\tau_{neq}} \boldsymbol{\sigma}'_{neq} \bar{\boldsymbol{F}}_i, \tag{23}$$

where $\boldsymbol{\sigma}'_{neq} = \bar{\boldsymbol{R}}_e^{\,T} \boldsymbol{\sigma}_{neq} \bar{\boldsymbol{R}}_e$. From Eq. (19), the evolution of damage is an energy dissipation process (i.e., $-\rho \frac{\partial \psi}{\partial \phi} \dot{\phi} \geq 0$). To satisfy the inequality, when $\dot{\phi} > 0$, $\frac{\partial \psi}{\partial \phi} < 0$, and when $\dot{\phi} = 0$, $\frac{\partial \psi}{\partial \phi} = 0$.

Here, the midpoint method is used to numerically obtain the inelastic deformation gradient at the end of a time increment, that is

$$\bar{\boldsymbol{F}}_i^{t+\frac{dt}{2}} = \bar{\boldsymbol{F}}_i^{t} + \frac{dt}{2} \dot{\bar{\boldsymbol{F}}}_i^{t}, \tag{24}$$

$$\bar{\boldsymbol{F}}_i^{t+dt} = \bar{\boldsymbol{F}}_i^{t} + dt \dot{\bar{\boldsymbol{F}}}_i^{t+\frac{dt}{2}}. \tag{25}$$

To calculate the elastic deformation gradient at the midpoint, it is required to find the total deformation gradient at the midpoint. This is done by taking the average of the deformation gradient at the start and end of the increment

$$\bar{\boldsymbol{F}}^{t+\frac{dt}{2}} = \frac{\bar{\boldsymbol{F}}^{t} + \bar{\boldsymbol{F}}^{t+dt}}{2}. \tag{26}$$

2.3 Phenomenological viscoelastic model coupled with a phase-field description

Following the additive decomposition of the free energy proposed in [1], the overall free energy of the material can be decomposed into an equilibrium ψ_{eq} , a non-equilibrium ψ_{neq}, and a volumetric part ψ_{vol} as:

$$\psi\left(\bar{\boldsymbol{B}}, \bar{\boldsymbol{B}}_e, J, \phi\right) = g(\phi)\psi_0^{+}\left(\bar{\boldsymbol{B}}, \bar{\boldsymbol{B}}_e, J\right) + \psi_0^{-}\left(\bar{\boldsymbol{B}}, \bar{\boldsymbol{B}}_e, J\right), \tag{27}$$

where

$$\psi_0^{+} = \psi_{eq}\left(\bar{\boldsymbol{B}}\right) + \psi_{neq}\left(\bar{\boldsymbol{B}}_e\right) + H(J-1)\psi_{vol}(J), \tag{28}$$

and

$$\psi_0^{-} = (1 - H(J-1))\psi_{vol}(J). \tag{29}$$

The Heaviside step function is defined as

$$H(x) = \begin{cases} 0, & x < 0 \\ 1, & x \geq 0 \end{cases}. \tag{30}$$

The energetic degradation function $g(\phi)$ captures the evolution of the strain energy versus the phase-field parameter and satisfies the following conditions:

$$g(0) = 1,\ g(1) = 0,\ g'(\phi) \leq 0 \text{ and } g'(1) = 0. \tag{31}$$

The conditions prescribe a monotonic decreasing behavior during the fracture evolution. To prevent crack propagation under compression, the volumetric strain energy does not change when $J < 1$ in Eqs. (28) and (29).

Here, the equilibrium ψ_{eq} and non-equilibrium ψ_{neq} parts of the free energy are defined by the neo-Hookean hyperelastic model as

$$\rho_0 \psi_{eq} = \frac{1}{2} \mu_{eq}\left(\nu_{np}, \Theta, w_w\right)\left(I_1\left(\bar{\boldsymbol{B}}\right) - 3\right), \tag{32}$$

and

$$\rho_0 \psi_{neq} = \frac{1}{2} \mu_{neq}\left(\nu_{np}, \Theta, w_w\right)\left(I_1\left(\bar{\boldsymbol{B}}_e\right) - 3\right), \tag{33}$$

where $I_1(\cdot) = \mathrm{tr}[\cdot]$ is the first invariant of the tensor. The material parameters μ_{eq} and μ_{neq} depend on temperature, BNP volume fraction ν_{np}, and water content w_w

$$\mu_{eq}\left(\nu_{np}, \Theta, w_w\right) = X\left(\nu_{np}, w_w\right)\mu_{eq}^0(\Theta), \tag{34}$$

$$\mu_{neq}\left(\nu_{np}, \Theta, w_w\right) = X\left(\nu_{np}, w_w\right)\mu_{neq}^0(\Theta). \tag{35}$$

Assuming that BNPs are well-dispersed rigid particles in the epoxy matrix, the Guth–Gold model is adopted by which the effective stiffness of particle-filled solids is obtained by $\langle E \rangle = XE_m$ [27]. The amplification factor X is typically a function of fillers' volume fraction and distribution. So far, some attempts of various levels of sophistication have been conducted to incorporate the effect of particle/matrix interactions on the effective modulus of polymer composites. Most of these models suggest a polynomial series expansion for the amplification factor. Here, a modified Guth–Gold model is proposed to account for uniformly distributed nanoparticles and moisture content as follows:

$$X = \left(1 + a_w w_w + b_w w_w^2\right)\left(1 + 3.5\nu_{np} + 18\nu_{np}^2\right). \tag{36}$$

In Eq. (36), the effect of moisture content on the material behavior is included based on the experimental data reported in the literature [16]. Accordingly, moisture absorption results in volumetric swelling, which in turn leads to an epoxy network with higher structural mobility and lower stiffness. However, the modulus is partially recovered beyond a certain moisture content. This effect can be explained by type II bound water [66]. Compared with the mobile water (no hydrogen bond) and type I bound water (forming one hydrogen bond), type II bound water molecules form two hydrogen bonds with epoxy chains. As a result, more type II water binds with the polymer chains during the water absorption process, resulting in higher cross-linking and stiffness partially retrieving. In this study, we choose a widely used model and modified the model to capture the effect of BNPs and water molecules as well-dispersed particles in an epoxy system.The modified amplification factor proposed in this work is a first step to capture the stress–strain behavior of BNP/epoxy nanocomposites under hygrothermal conditions.

To consider the effect of temperature on the material properties, a modified Kitagawa model proposed by Unger et al. [60] is utilized with the following equations:

$$\mu_{eq}^{0} = \mu_{eq,ref}^{0}\left(2 - \exp\left[\alpha\left(\Theta - \Theta_{ref}\right)\right]\right), \tag{37}$$

$$\mu_{neq}^{0} = \mu_{neq,ref}^{0}\left(2 - \exp\left[\alpha\left(\Theta - \Theta_{ref}\right)\right]\right). \tag{38}$$

The volumetric part of the free energy ψ_{vol} is also defined by

$$\rho_0\psi_{vol} = \frac{1}{2}k_v\left(\nu_{np}\right)\left(\frac{J_m^2 - 1}{2} - \ln\left[J_m\right]\right)^2, \tag{39}$$

where the bulk modulus is assumed to be $k_v = \left(2 - \exp\left[\alpha\left(\Theta - \Theta_{ref}\right)\right]\right)X\left(\nu_{np}\right)k_v^0$. The corresponding stresses are then obtained from

$$\begin{cases} \boldsymbol{\sigma} = g\boldsymbol{\sigma}_{dev} + \boldsymbol{\sigma}_{vol} & J < 1, \\ \boldsymbol{\sigma} = g\boldsymbol{\sigma}_{dev} + g\boldsymbol{\sigma}_{vol} & J \geq 1, \end{cases} \tag{40}$$

where

$$\boldsymbol{\sigma}_{dev} = J^{-1}\left(\mu_{eq}\bar{\boldsymbol{B}}^{D} + \mu_{neq}\bar{\boldsymbol{B}}_{e}^{D}\right), \tag{41}$$

and

$$\boldsymbol{\sigma}_{vol} = \frac{1}{2}k_v J_{\Theta}^{-1}\left(J_m - \frac{1}{J_m}\right)\mathbf{1}. \tag{42}$$

3 Phase-field model at finite deformation

To evaluate the predictive capability of the proposed material model, we use the model to develop a PFM formulation for nanoparticle/polymer composites. This section presents a variational phase-field formulation for fracture at finite deformation. In the following, to show the procedure of analysis, we derive the continuum mechanics incremental scheme and FE equations.

3.1 Problem field description

The strong form of the boundary value problem in spatial description for the coupling between displacement $\boldsymbol{u}$ and phase-field variable ϕ can be written as

$$\begin{cases} \boldsymbol{\nabla}.\boldsymbol{\sigma} + \boldsymbol{b} = 0 \\ \frac{G_c}{l_0}\phi - G_c l_0 \Delta\phi = -g'(\phi)\mathcal{H} \end{cases} \text{in} \quad \Omega, \tag{43}$$

with the following boundary conditions:

$$\begin{cases} \boldsymbol{\sigma}.\boldsymbol{n} = \boldsymbol{t} & \text{on} \quad \Gamma_t, \\ \boldsymbol{u} = \boldsymbol{u}_d & \text{on} \quad \Gamma_u, \\ \nabla\phi.\boldsymbol{n} = 0 & \text{on} \quad \Gamma, \end{cases} \tag{44}$$

where l_0 is the length scale that controls the width of the diffuse crack, $\Gamma = \Gamma_t \cup \Gamma_u$, $\boldsymbol{b}$ represents the vector of body forces, $\boldsymbol{n}$ is the outward unit normal vector on the boundary Γ of the body Ω, $\boldsymbol{t}$ is the traction force, and $\boldsymbol{u}_d$ represents the prescribed displacements at the boundary Γ_u. To take into account the effect of BNP content on the fracture evolution in the nanocomposites, the energy release rate is taken to be $G_c = X\left(\nu_{np}, w_w\right)G_c^0$. Following Miehe et al. [44], $\mathcal{H}$ is the local history field of maximum positive reference energy defined by:

$$\mathcal{H}(t) = \max_{\tau\in[0,t]}\psi_0^{+}\left(\bar{\boldsymbol{B}}, \bar{\boldsymbol{B}}_e, J\right), \tag{45}$$

which prevents the healing of cracks when the source term ψ_0^{+} decreases. Here, a monotonically decreasing degradation function $g(\phi)$, satisfying conditions presented in Eq. (31), is chosen [29]

$$g(\phi) = \left(a_g - 2\right)(1-\phi)^3 + \left(3 - a_g\right)(1-\phi)^2 + k;\ a_{g\geq 0}, \tag{46}$$

where k is a small positive parameter introduced for ensuring for the stability of the solution [44].

It should be noted that the propagation of cracks in the benchmark tests investigated in the present study takes a few minutes to a few days depending on the displacement rate. While moisture diffusion into a specimen and the degradation of its mechanical properties due to water

absorption takes some weeks to some months [16]. It implies that moisture diffusion and crack propagation can be considered decoupled phenomena physically.

3.2 Finite-element formulation

To derive the governing equations in weak form, the weighted residual approach is used. Thus, Eq. (43) is multiplied by weight functions and integrated over Ω as

$$\int_{\Omega} \mathbf{w}_u.(\boldsymbol{\nabla}.\boldsymbol{\sigma} + \mathbf{b})\mathrm{d}\Omega = 0 \quad \forall \quad \mathbf{w}_u \in H_0^1(\Omega), \tag{47}$$

and

$$\int_{\Omega} w_\phi \left(g'(\phi)\mathcal{H} + \frac{G_c}{l_0}\phi - G_c l_0 \Delta\phi \right)\mathrm{d}\Omega = 0 \quad \forall \quad w_\phi \in H^1(\Omega). \tag{48}$$

Using the divergence theorem and imposing the boundary conditions $\boldsymbol{\sigma}.\boldsymbol{n} = \boldsymbol{t}$ and $\nabla\phi.\boldsymbol{n} = 0$ presented in Eq. (44), the weak form of the governing equations can be written as follows:

$$\int_{\Omega} \boldsymbol{\nabla}\mathbf{w}_u : \boldsymbol{\sigma}\mathrm{d}\Omega = \int_{\Omega} \mathbf{w}_u.\mathbf{b}\mathrm{d}\Omega + \int_{\Gamma} \mathbf{w}_u.\mathbf{t}\mathrm{d}\Gamma, \tag{49}$$

$$\int_{\Omega} \left(w_\phi g'(\phi)\mathcal{H} + \frac{G_c}{l_0} w_\phi \phi + G_c l_0 \nabla w_\phi.\nabla\phi \right)\mathrm{d}\Omega = 0. \tag{50}$$

Employing the Bubnov–Galerkin method, the displacement, the phase-field field, and the corresponding weight functions are discretized in each element

$$\begin{aligned} &\mathbf{u}^h = \mathbf{N}_u\mathbf{u}, \quad \mathbf{w}_u^h = \mathbf{N}_u\mathbf{w}_u, \quad w_\phi^h = \mathbf{N}_\phi\mathbf{w}_\phi, \quad \phi^h = \mathbf{N}_\phi\boldsymbol{\phi}, \\ &\boldsymbol{\nabla}\mathbf{w}_u^h = \mathbf{B}_u\mathbf{w}_u, \quad \nabla w_\phi^h = \mathbf{B}_\phi\mathbf{w}_\phi, \quad \nabla\phi^h = \mathbf{B}_\phi\boldsymbol{\phi}, \end{aligned} \tag{51}$$

where the shape function matrices $\boldsymbol{N}_u$ and $\boldsymbol{N}_\phi$ interpolate the nodal values $\boldsymbol{u}$ and $\boldsymbol{\phi}$, respectively, and $\boldsymbol{B}_u$ and $\boldsymbol{B}_\phi$ are the gradient operators for the displacement and the nonlocal equivalent strain, respectively. The same shape functions interpolate the nodal values of the weight functions $\mathbf{w}_u$ and $\mathbf{w}_\phi$. Substituting the relations into the weak formulation of the governing equations yields

$$\int_{\Omega} \mathbf{w}_u^T\mathbf{B}_u^T\boldsymbol{\sigma}\mathrm{d}\Omega = \int_{\Omega} \mathbf{w}_u^T\mathbf{N}_u^T\mathbf{b}\mathrm{d}\Omega + \int_{\Gamma} \mathbf{w}_u^T\mathbf{N}_u^T\mathbf{t}\mathrm{d}\Gamma, \tag{52}$$

$$\int_{\Omega} \mathbf{w}_\phi^T \left(g'(\phi)\mathcal{H}\mathbf{N}_\phi^T + \frac{G_c}{l_0}\mathbf{N}_\phi^T\mathbf{N}_\phi\boldsymbol{\phi} + G_c l_0 \mathbf{B}_\phi^T\mathbf{B}_\phi\boldsymbol{\phi} \right)\mathrm{d}\Omega = 0, \tag{53}$$

which have to hold for any choice of $\mathbf{w}_u$ and $\mathbf{w}_\phi$. The discretized equations can therefore be rewritten as

$$\int_{\Omega} \mathbf{B}_u^T\boldsymbol{\sigma}\mathrm{d}\Omega = \int_{\Omega} \mathbf{N}_u^T\mathbf{b}\mathrm{d}\Omega + \int_{\Gamma} \mathbf{N}_u^T\mathbf{t}\mathrm{d}\Gamma, \tag{54}$$

$$\int_{\Omega} \left(g'(\phi)\mathcal{H}\mathbf{N}_\phi^T + \frac{G_c}{l_0}\mathbf{N}_\phi^T\mathbf{N}_\phi\boldsymbol{\phi} + G_c l_0 \mathbf{B}_\phi^T\mathbf{B}_\phi\boldsymbol{\phi} \right)\mathrm{d}\Omega = 0. \tag{55}$$

The equations can then be expressed in terms of external and internal nodal forces as

$$\mathbf{f}_{int}^u = \mathbf{f}_{ext}^u \quad \text{and} \quad \mathbf{f}_{int}^\phi = \mathbf{f}_{ext}^\phi, \tag{56}$$

where

$$\mathbf{f}_{int}^u = \int_{\Omega} \mathbf{B}_u^T\boldsymbol{\sigma}\mathrm{d}\Omega, \tag{57}$$

$$\mathbf{f}_{ext}^u = \int_{\Omega} \mathbf{N}_u^T\mathbf{b}\mathrm{d}\Omega + \int_{\Gamma} \mathbf{N}_u^T\mathbf{p}\mathrm{d}\Gamma, \tag{58}$$

$$\mathbf{f}_{int}^\phi = \int_{\Omega} \left(g'(\phi)\mathcal{H}\mathbf{N}_\phi^T + \frac{G_c}{l_0}\mathbf{N}_\phi^T\mathbf{N}_\phi\boldsymbol{\phi} + G_c l_0 \mathbf{B}_\phi^T\mathbf{B}_\phi\boldsymbol{\phi} \right)\mathrm{d}\Omega, \tag{59}$$

$$\mathbf{f}_{ext}^\phi = \mathbf{0}. \tag{60}$$

3.3 Consistent incremental-iterative scheme

By linearizing Eq. (56) at iteration $i+1$ with respect to the previous iteration i, a consistent tangent stiffness is obtained as follows:

$$\mathbf{f}_{ext}^u = \mathbf{f}_{int,i}^u + \delta\mathbf{f}_{int}^u, \tag{61}$$

$$\mathbf{f}_{ext}^\phi = \mathbf{f}_{int,i}^\phi + \delta\mathbf{f}_{int}^\phi. \tag{62}$$

The linearized equations are finally summarized as follows:

$$\begin{bmatrix} \mathbf{K}_i^{uu} & \mathbf{K}_i^{u\phi} \\ \mathbf{K}_i^{\phi u} & \mathbf{K}_i^{\phi\phi} \end{bmatrix} \begin{bmatrix} \delta\mathbf{u}_{i+1} \\ \delta\boldsymbol{\phi}_{i+1} \end{bmatrix} = \begin{bmatrix} \mathbf{f}_{ext}^u \\ \mathbf{f}_{ext}^\phi \end{bmatrix} - \begin{bmatrix} \mathbf{f}_{int,i}^u \\ \mathbf{f}_{int,i}^\phi \end{bmatrix}, \tag{63}$$

where

$$\mathbf{K}_i^{uu} = \int_{\Omega} \mathbf{B}_u^T \left(\frac{\partial\boldsymbol{\sigma}}{\partial\boldsymbol{\varepsilon}} \right)\mathbf{B}_u\mathrm{d}\Omega + \int_{\Omega} \mathbf{B}_u^T\boldsymbol{\sigma}\mathbf{B}_u\mathrm{d}\Omega, \tag{64}$$

$$\mathbf{K}_i^{u\phi} = \int_{\Omega} \mathbf{B}_u^T \left(\frac{\partial\boldsymbol{\sigma}}{\partial\phi} \right)\mathbf{N}_\phi\mathrm{d}\Omega, \tag{65}$$

$$\mathbf{K}_i^{\phi u} = \int_{\Omega} \mathbf{N}_\phi^T \left(g'\frac{\partial\mathcal{H}}{\partial\boldsymbol{\varepsilon}} \right)\mathbf{B}_u\mathrm{d}\Omega, \tag{66}$$

$$\mathbf{K}_i^{\phi\phi} = \int_\Omega J^{-1}\left(\mathbf{N}_\phi^T\left(g''\mathcal{H} + \frac{G_c}{l_0}\right)\mathbf{N}_\phi + G_c l_0 \mathbf{B}_\phi^T \mathbf{B}_\phi\right) \mathrm{d}\Omega \text{ and} \tag{67}$$

$$\mathbf{g}_i = \begin{bmatrix} \mathbf{f}_{ext}^u \\ \mathbf{f}_{ext}^\phi \end{bmatrix} - \begin{bmatrix} \mathbf{f}_{int,i}^u \\ \mathbf{f}_{int,i}^\phi \end{bmatrix}. \tag{68}$$

Generally, two approaches have been suggested to solve the phase-field–displacement system of equations: simultaneously solving $\mathbf{u}$ and $\boldsymbol{\phi}$ (monolithic algorithm) and sequentially solving $\mathbf{u}$ and ϕ as coupled staggered fields. However, it is known that monolithic schemes poorly perform in solving Eq. 63, since the energy functional is non-convex with respect to the unknowns [11]. This non-convexity causes the Jacobian matrix in the Newton method to become indefinite, preventing convergence and robustness in monolithic solutions. On the other hand, although staggered algorithms are relatively robust, the time increment must be adequately small to prevent deviating from the equilibrium path. To make a trade-off between robustness and efficiency, a monolithic solution scheme based on the Broyden–Fletcher–Goldfarb–Shanno (BFGS) algorithm has been proposed in the literature to solve the system of coupled equations [34, 64]. In this work, the BFGS method presented in the following section is considered as the primary solution scheme.

3.4 The Broyden–Fletcher–Goldfarb–Shanno algorithm

In quasi-Newton methods, the stiffness matrix is replaced by an approximation of the stiffness $\widetilde{\mathbf{K}}$. The approximated stiffness matrix satisfies the quasi-Newton equation as follows:

$$\widetilde{\mathbf{K}}\delta\mathbf{z} = \delta\mathbf{g}, \tag{69}$$

where

$$\boldsymbol{\delta z} = \begin{bmatrix} \delta\mathbf{u}_{i+1} \\ \delta\boldsymbol{\phi}_{i+1} \end{bmatrix} \text{ and} \tag{70}$$

$$\boldsymbol{\delta g} = \mathbf{g}_{i+1} - \mathbf{g}_i. \tag{71}$$

The quasi-Newton method is an algorithmic secant method based on the series of successive approximations to the solution, which finds the root of nonlinear equations using the current and previous iteration steps. In the BFGS quasi-Newton method, the approximated stiffness matrix is updated by its predecessor and a correction matrix of rank 2

$$\widetilde{\mathbf{K}} = \widetilde{\mathbf{K}}_i - \frac{\left(\widetilde{\mathbf{K}}_i\delta\mathbf{z}\right)\left(\widetilde{\mathbf{K}}_i\delta\mathbf{z}\right)^T}{\delta\mathbf{z}^T\widetilde{\mathbf{K}}_i\delta\mathbf{z}} + \frac{\delta\mathbf{g}\delta\mathbf{g}^T}{\delta\mathbf{z}^T\delta\mathbf{g}}. \tag{72}$$

It can be shown that a symmetric and positive-definite initial guess $\widetilde{\mathbf{K}}_0$ leads to the symmetric and positive-definite updated one [39]. Therefore, since the stiffness matrix in Eq. 63 is not necessarily symmetric and positive-definite, an uncoupled stiffness matrix is taken as the initial guess

$$\widetilde{\mathbf{K}}_0 = \begin{bmatrix} \mathbf{K}_0^{uu} & \mathbf{0} \\ \mathbf{0} & \mathbf{K}_0^{\phi\phi} \end{bmatrix}. \tag{73}$$

In the above equation, $\mathbf{K}_0^{uu}$ is symmetric and positive-definite. Also, $\mathbf{K}_0^{\phi\phi}$ is symmetric and positive-definite for an appropriate length-scale parameter. Accordingly, the approximated stiffness matrix given by the BFGS algorithm is symmetric and positive-definite. It should be noted that although the off-diagonal inter-field coupling terms have been dropped in Eq. 73, the approximation 72 couples the $\mathbf{u}$ and $\boldsymbol{\phi}$ fields. This is not the case for Newton-based monolithic algorithms adopted for solving weakly coupled problems.

The BFGS algorithm along with a line search method helps to prevent divergence of equilibrium iterations resulting from the inexact stiffness matrix. Therefore, the solution is updated as follows:

$$\mathbf{z}_{i+1} = \mathbf{z}_i + s\delta\mathbf{z}, \tag{74}$$

where the multiplier s is chosen in the way that component of $\mathbf{g}$ in the search direction is zero with a tolerance

$$\delta\mathbf{z}^T\mathbf{g}_{i+1} = 0. \tag{75}$$

Here, convergence is assumed to be achieved if both the residual and solution correction controls are met, that is

$$g_{max}^\alpha \le \epsilon_g \widetilde{g}^\alpha \text{ and} \tag{76}$$

$$c_{max}^\alpha \le \epsilon_c \Delta z_{max}, \tag{77}$$

where g_{max}^α is the largest residual in the balance equations for the displacement field ($\alpha = u$) and the phase-field ($\alpha = \phi$), $\widetilde{g}^\alpha$ is the overall time-averaged flux for the displacement and phase-field obtained during the current time step including the current increment, c_{max}^α is the largest correction to the field variable α given by the current iteration, and Δz_{max} is the largest incremental change to the corresponding solution variable in the current time increment. Here, the tolerances are taken to be $\epsilon_g = 0.01$ and $\epsilon_c = 0.01$. The implementation of the BFGS algorithm is outlined in Table 1.

3.5 Consistent tangent moduli based on the Jaumann-Zaremba stress rate

To integrate the viscoelastic model into the incremental-iterative FE framework, the tangent modulus tensor

Table 1 BFGS algorithm for the system of coupled equations

1. Initialize the iteration process.
   (a) Set initial parameters: $i = 0$.
   (b) Initial stiffness matrix $\tilde{\mathbf{K}}_0$, $\mathbf{z}_0$.
2. Loop on i for equilibrium.
   (a) Compute search direction $\delta\mathbf{z}$ using Eq. (69).
   (b) Line search and solution vector update:
      i. Compute $G(0) = \delta\mathbf{z}^T\mathbf{g}(\mathbf{z}_i)$
      ii. Loop over $s \in s_k = \{1, 2, 4, 8, 16\}$
         – Compute $G(s) = \delta\mathbf{z}^T\mathbf{g}(\mathbf{z}_i + s\delta\mathbf{z})$
         – IF $G(s) \leq$ STOL$*G(0)$ THEN go to step iii
         – IF the sign of $G(s)$ changes THEN
            Finer adjustment of $s \in s_{k-1}, s_k$ using the accelerated secant method (Illinois algorithm [39])
         ENDIF
      iii. Update the solution using Eq. 74
   (c) Equilibrium check using Eqs. (76) and (76)
      – IF the convergence criteria are achieved THEN EXIT
   (d) Increment iteration counter: $i = i + 1$
   (e) Stability check
      i. Compute the condition number $c = \sqrt{\frac{sG(0)}{G(0)-G(s)}}$
      ii. IF $c > c_{crit} \approx 5$ THEN
         – Take previous quasi-secant matrix $\tilde{\mathbf{K}}_i = \tilde{\mathbf{K}}_{i-1}$
         – go to 2a
   (f) Update the stiffness matrix using the BFGS algorithm (see Eq. (72))

$\mathbb{C}^{\sigma J} = \frac{\partial \boldsymbol{\sigma}}{\partial \boldsymbol{\epsilon}}$ needs to be explicitly specified. However, a closed-form calculation of the tangent tensor is not a straightforward task. Here, we use an efficient numerical approximation of the tangent moduli proposed by Sun et al. [58]. In this approach, by perturbing the deformation gradient, the tangent moduli for the Jaumann rate of the Cauchy stress are accurately approximated by a forward difference of the Cauchy stresses. The Jaumann rate of the Cauchy stress can be expressed as

$$\overset{\triangledown}{\boldsymbol{\sigma}} = \dot{\boldsymbol{\sigma}} - \boldsymbol{W}\boldsymbol{\sigma} - \boldsymbol{\sigma}\boldsymbol{W}^T = \mathbb{C}^{\sigma J} : \boldsymbol{D}. \tag{78}$$

The linearized incremental form of Eq. (78) is then obtained from

$$\boldsymbol{\Delta\sigma} - \boldsymbol{\Delta W}\boldsymbol{\sigma} - \boldsymbol{\sigma}\boldsymbol{\Delta W}^T = \mathbb{C}^{\sigma J} : \boldsymbol{\Delta D}. \tag{79}$$

To numerically calculate components of $\mathbb{C}^{\sigma J}$, Eq. (79) is perturbed by applying small perturbations to components of $\boldsymbol{\Delta D}$ and $\boldsymbol{\Delta W}$ tensors. Here, $\boldsymbol{\Delta W}_{ij}$ and $\boldsymbol{\Delta D}_{ij}$ tensors with perturbed (i,j) components are expressed as

$$\boldsymbol{\Delta W}_{ij} = \frac{1}{2}\left(\boldsymbol{\Delta F}_{ij}\boldsymbol{F}^{-1} - \left(\boldsymbol{\Delta F}_{ij}\boldsymbol{F}^{-1}\right)^T\right), \tag{80}$$

and

$$\boldsymbol{\Delta D}_{ij} = \frac{1}{2}\left(\boldsymbol{\Delta F}_{ij}\boldsymbol{F}^{-1} + \left(\boldsymbol{\Delta F}_{ij}\boldsymbol{F}^{-1}\right)^T\right), \tag{81}$$

where the corresponding perturbed $\boldsymbol{\Delta F}_{ij}$ is obtained from perturbing its (i,j) component as [41]

$$\boldsymbol{\Delta F}_{ij} = \frac{\epsilon}{2}\left(e_i \otimes e_j\boldsymbol{F} + e_j \otimes e_i\boldsymbol{F}\right), \tag{82}$$

where ϵ is a small perturbation parameter. By substituting Eq. (82) into Eqs. (80) and (81), we have

$$\boldsymbol{\Delta W}_{ij} = \boldsymbol{0}, \tag{83}$$

$$\boldsymbol{\Delta D}_{ij} = \frac{\epsilon}{2}\left(e_i \otimes e_j + e_j \otimes e_i\right). \tag{84}$$

It is noteworthy that $\boldsymbol{\Delta D}$ has six independent components due to its symmetry. Therefore, the choice of (i,j) would be (1,1), (2,2), (3,3), (1,2), (1,3), and (2,3). The perturbed deformation gradient $\hat{\boldsymbol{F}}_{ij}$ can then be written as

$$\hat{\boldsymbol{F}}_{ij} = \boldsymbol{F} + \boldsymbol{\Delta F}_{ij}. \tag{85}$$

Using Eq. (85), $\boldsymbol{\Delta\sigma}$ is approximated by the forward difference of the perturbed and unperturbed Cauchy stresses

$$\boldsymbol{\Delta\sigma} \approx \boldsymbol{\sigma}\left(\hat{\boldsymbol{F}}_{ij}\right) - \boldsymbol{\sigma}(\boldsymbol{F}). \tag{86}$$

Substituting Eqs. (83), (84), and (86) into Eq. (79) gives

$$\boldsymbol{\sigma}\left(\hat{\boldsymbol{F}}_{ij}\right) - \boldsymbol{\sigma}(\boldsymbol{F}) \approx \mathbb{C}^{\sigma J}_{ij} : \frac{\epsilon}{2}\left(e_i \otimes e_j + e_j \otimes e_i\right). \tag{87}$$

Using Eq. (87), the numerical approximation of the tangent moduli is finally obtained as

$$\mathbb{C}^{\sigma J}_{ij} = \frac{1}{\epsilon}\left[\boldsymbol{\sigma}\left(\hat{\boldsymbol{F}}_{ij}\right) - \boldsymbol{\sigma}(\boldsymbol{F})\right], \tag{88}$$

where $\mathbb{C}^{\sigma J}_{ij}$ represents the components of the tangent modulus tensor $\mathbb{C}^{\sigma J}$ calculated by the perturbation of $\boldsymbol{\Delta F}_{ij}$.

4 Fracture experiments and numerical simulations

In the following section, the potential of the quasi-Newton method-based monolithic algorithm in achieving convergence and reducing the computation time of the rate-dependent fracture of solids is first investigated. The numerical results of CT tests of BNP/epoxy samples are then compared with the experimental data to identify the material parameters required for the proposed PFM. Next, the effect of hygrothermal conditions and deformation rate on the fracture behavior of the polymer nanocomposites is studied. Finally, the model's capability in predicting fracture patterns is qualitatively assessed using single-edge notched tests.

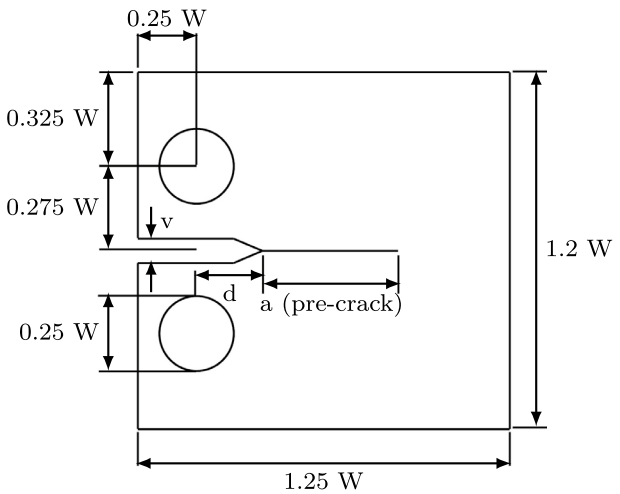

Fig. 2 Planar dimensions of the CT specimen with a thickness of 5 mm ($W = 35$ mm, $d = 6$ mm, and $a = 16$ mm)

4.1 Experiments

To prepare the nanocomposite specimens, BNPs are first mixed with an epoxy resin. The epoxy system chosen in this study is a commercially available amine-cured epoxy system from Olin Epoxy, namely the epoxy resin of type AIRSTONE 880E and the hardener of type AIRSTONE 886H with an epoxy–hardener mixing ratio of 100:31 by weight. A dispersion process is then conducted to break up nanoparticle agglomerates under mechanical shear loading using a three-roll mill (Exakt, 80E). The dispersion process ensures that nanoparticles are well dispersed in the epoxy matrix. The mixture is next de-gassed at room temperature and poured into a mold for curing nanocomposite plates. The curing process is performed at 353 K for 5 h. The mass density and glass-transition temperature of the epoxy are 1.2 g/cc and 355 K, respectively. The plates are cut into CT specimens with a width of 35 mm and a nominal thickness of 5 mm using a CNC milling machine according to DIN EN ISO 13586. A pre-crack with a length of 16 mm is introduced into the notch root by forcing a razor blade. The pre-crack ensures that a crack is formed ahead of the razor blade tip. The specifications of the specimen are illustrated in Fig. 2. Fracture toughness experiments are carried out at a deformation rate of 10 mm/min and 296 K. Since experimental results may be affected by uncertainties resulting from the manufacturing process, each force–displacement response is obtained from five CT tests to secure the experimental data statistically.

4.2 Simulations

We first study the crack growth in a CT specimen. The specimen specifications and dimensions in mm are illustrated in Fig. 2. Considering the symmetry at the mid-length of the specimen, the FE analysis of half of the specimen using symmetric boundary conditions would provide a complete solution of the full model with less computational cost. Loading and boundary conditions of the reduced model are

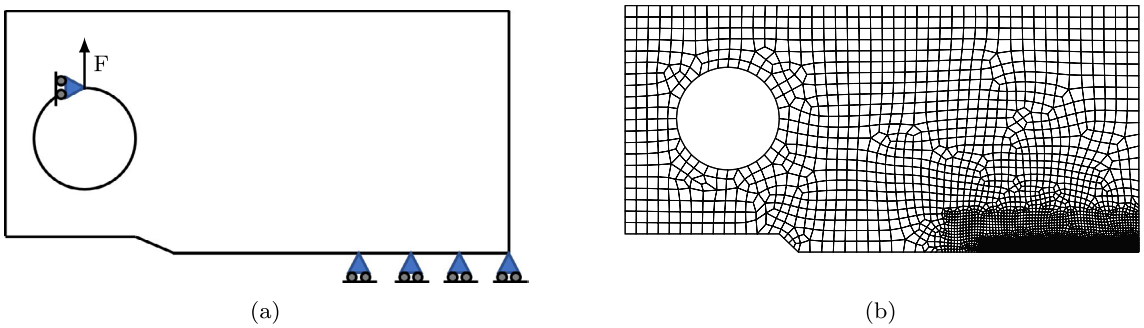

Fig. 3 **a** Loading and boundary conditions imposed on half of the CT specimen due to symmetry, and **b** two-dimensional FE model composed of 6130 Q4 elements with 6334 nodes (fine mesh)

Table 2 Material parameters of the proposed PFM

	Parameter	Value	References
Equilibrium part (Eq. (37))	$\mu^0_{eq,ref}$ (MPa)	800	
Non-equilibrium part (Eq. (38))	$\mu^0_{neq,ref}$ (MPa)	2100	
Viscoelastic dashpot (Eq. (22))	$\dot{\epsilon}_0$ (s^{-1})	8.9207×10^{11}	[59]
	τ_0 (MPa)	140.65	[59]
	ΔH (J)	2.0324×10^{-19}	[59]
Modified Kitagawa parameters (Eqs. (37) and (38))	α (K^{-1})	0.01093	[60]
	Θ_{ref} (K)	296	[60]
Volumetric part (Eq. (40))	k^0_v (MPa)	1200	
Thermal expansion coefficient (Eq. (3))	α_Θ (K^{-1})	4.19×10^{-5}	[60]
Moisture swelling coefficient (Eq. (4))	α_w	0.039	Adopted based on [16]
Energy release rate (Eq. (43))	G^0_c (N/mm)	250×10^{-3}	
Degradation function parameter (Eq. (46))	a_g	1	

shown in Fig. 3a. The following simulations are performed under plane strain conditions, and the load is applied in the form of a monotonic displacement with constant displacement increments. The material parameters are presented in Table 2. The model is discretized with four-noded quadrilateral (Q4) elements. Figure 3b shows the corresponding mesh with 6130 Q4 elements. Due to stress and strain concentrations at the bottom-right part of the model, the mesh is refined toward the part, so that the characteristic element size of the fine-level discretization is eight times smaller than the phase-field length scale. In the following CT simulations, two times the vertical displacement of the point placed at the external force is used to measure the displacement.

The resulting force–displacement curves of the CT tests obtained from both the quasi-Newton monolithic and staggered solutions are shown in Fig. 4a. The load is applied to a neat epoxy sample at a constant deformation rate of $\dot{u} = 10$ mm/min, $\Theta = 296$ K and $w = 0$. In the monolithic solution, the load is applied with a constant displacement increment of $\Delta u = 5 \times 10^{-3}$ mm. It can be seen that the staggered solution is sensitive to the increment size, and two orders of magnitude smaller displacement increment (i.e., $\Delta u = 5 \times 10^{-5}$ mm) is required to reproduce the monolithic solution. The cumulative number of iterations versus displacement is also presented in Fig. 4b. The simulation results show that recovering the monolithic result using a staggered solution requires a displacement increment of 5×10^{-5} mm and a total number of iterations that is one order of magnitude larger. The significant reduction in the number of iterations justifies the computational efficiency and applicability of the monolithic solution for studying rate-dependent fracture problems in polymer-based materials.

Next, CT simulation tests are performed to asses the predictive capability of the proposed PFM model in capturing

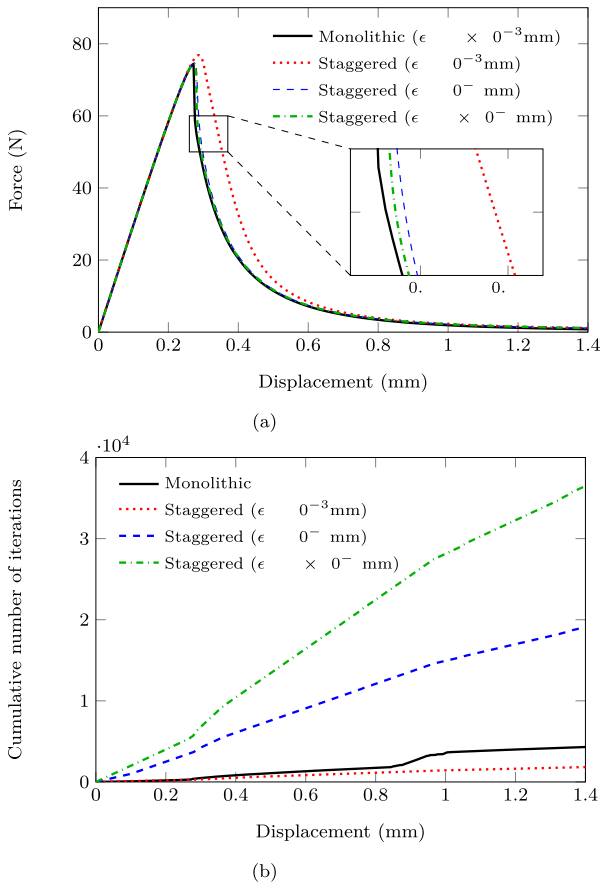

Fig. 4 **a** Force–displacement response for neat epoxy samples obtained by the quasi-Newton monolithic and staggered solvers at $\dot{u} = 10$ mm/min and $\Theta = 296$ K, and **b** a comparison of the cumulative number of iterations for the solvers

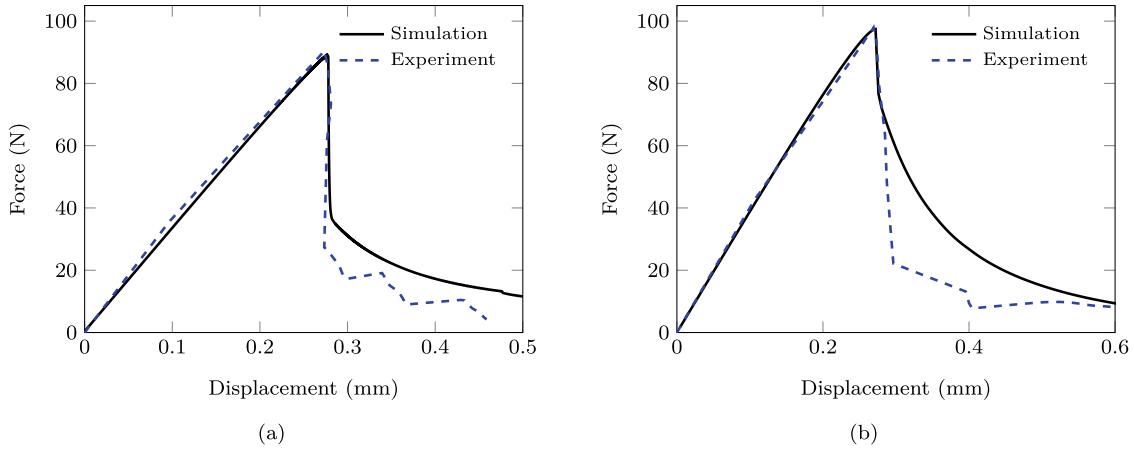

Fig. 5 Effect of BNP weight fraction on the force–displacement curve in the CT test at $\dot{u} = 10$ mm/min and $\Theta = 296$ K: (a) BNP(10 %wt)/epoxy sample, and (b) BNP(15 %wt)/epoxy sample

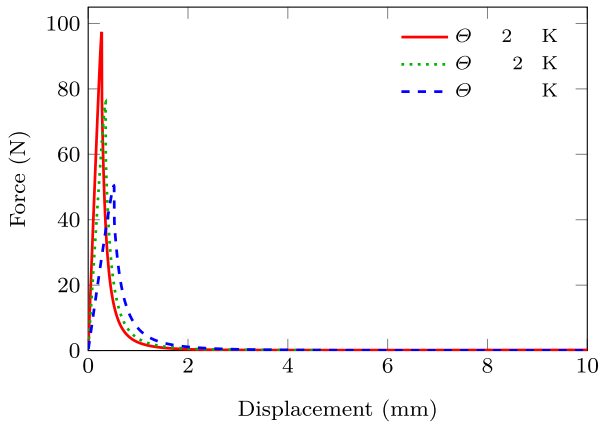

Fig. 6 Effect of temperature on the force–displacement curve in CT simulation tests of BNP(15 %wt)/epoxy samples at $\dot{u} = 10$ mm/min

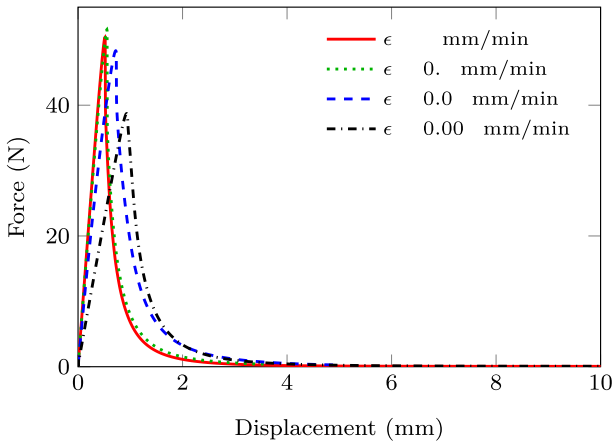

Fig. 7 Effect of deformation rate on the force–displacement curve in CT simulation tests of BNP(15 %wt)/epoxy samples at $\Theta = 346$ K

the fracture behavior of BNP/epoxy nanocomposites. Figures 5a and b show the force–displacement response associated with specimens made of BNP(10 %wt)/epoxy and BNP(15 %wt)/epoxy at the deformation rate of $\dot{u} = 10$ mm/min, $\Theta = 296$ K, and $w = 0$. The mass density of the neat epoxy and BNPs are 1.2 and 3.0 g/cc, respectively. Accordingly, the volume fractions are obtained to be $v_{np} = 0.043$ and 0.065 for 10 and 15 %wt of BNPs, respectively. The simulations are performed using the material parameters listed in Table 2. The effect of nanoparticle contents is also considered using the modified Guth–Gold model presented in Sect. 2. The agreement between experimental data and numerical predictions in the figures confirms the predictive capability of the PFM in capturing the effect of nanoparticles on the fracture behavior of the nanocomposites. Also, from Figs. 4a and 5, it can be found that the peak force increases from 75.29 N for neat epoxy to 90.26 and 97.94 N for nanocomposites with 10 and 15 %wt of BNP contents, respectively. The results indicate that the critical load for crack initiation increases by 30% by increasing the BNP content to 15 %wt.

We then study the effect of temperature on the fracture behavior of BNP/epoxy nanocomposites. Figure 6 shows the force–displacement response in CT simulation tests of specimens with 15 wt% of BNPs. Here, the deformation rate is kept constant at $\dot{u} = 10$ mm/min, while temperature varies from $\Theta = 296$ to 346 K. The simulation results show that the peak force decreases from around 98 to 51 N by increasing temperature from 296 to 346 K. Furthermore, the displacement at the fracture initiation rises from 0.27 to 0.53 mm by increasing temperature from 296 to 346 K. The simulation results can be explained as follows. First, the shear and bulk modulus associated with the equilibrium, non-equilibrium, and volumetric responses decrease by increasing

temperature (see Eqs. (37) and (38)), leading to a less stiff material. Second, the nonlinear viscoelastic flow defined by the Argon model in Eq. (22) is temperature-dependent, so that the viscoelastic flow increases with an increase in temperature. As a result, a larger portion of the strain energy is dissipated at higher temperatures, leading to a smaller peak force and larger displacement at the fracture initiation. It is noteworthy that the effect of temperature on the energy release rate has not been considered in the simulations. Although this assumption may be acceptable in the studied range of temperatures according to experimental data [32], further studies are required to investigate the variation of energy release rate with temperature.

In Fig. 7, CT simulation tests are conducted to investigate the effect of the deformation rate ($\dot{u}$) on the fracture response of BNP (15 wt%)/epoxy nanocomposites. Here, temperature is set to be 346 K, and large deformations up to 10 mm at different deformation rates, varying from 0.001 to 1 mm/min, are applied to the specimens. From the figure, the displacement at the peak force decreases from 1.31 to 0.53 mm by increasing the deformation rates from 0.001 to 1 mm/min. In analogy with the effect of temperature, the viscous effect is smaller, and the dashpot behaves more like a solid at higher deformation rates. Therefore, a smaller portion of the strain energy is dissipated, and displacement at the fracture initiation and peak force become smaller. The evolution of damage in a BNP(15 %wt)/epoxy sample at the deformation rate of 0.01 mm/min and imposed displacements of 1, 2, 5, and 10 mm is illustrated in Figs. 8a–d.

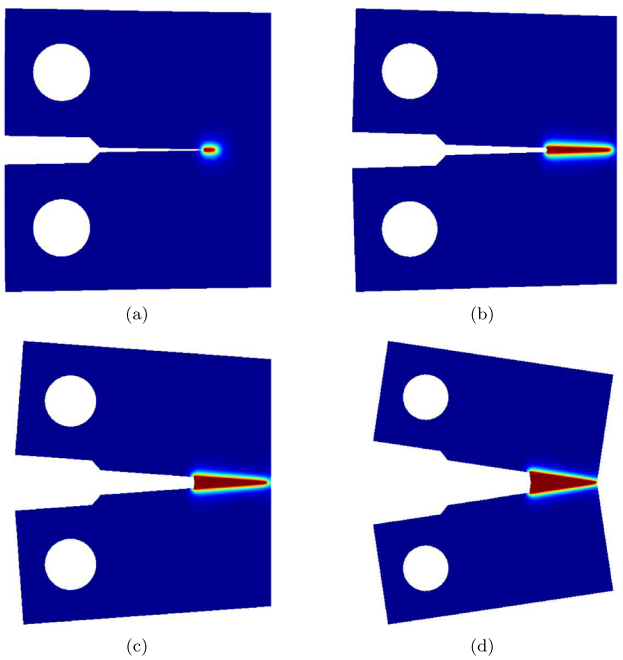

Fig. 8 Contour plots of damage in the CT simulation test of a BNP(15 %wt)/epoxy sample at 346 K and the deformation rate of 0.01 mm/min at the imposed displacement of **a** 1 mm, **b** 2 mm, **c** 5 mm, and **d** 10 mm

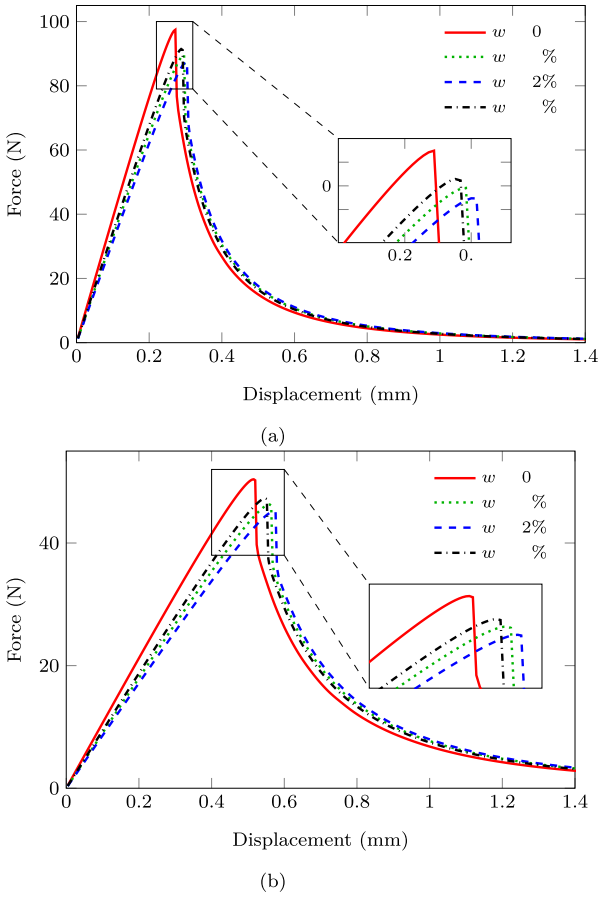

Fig. 9 Effect of moisture content on the force–displacement curve in CT simulation tests of BNP (15 %wt)/epoxy samples at **a** $\Theta = 296$ K and **b** $\Theta = 346$ K

In the following, we study the effect of moisture on the fracture behavior of the nanocomposites. Figures 9a and 9b show the force–displacement response in CT simulation tests of specimens with 15 wt% of BNPs at 296 and 346 K, respectively. In the simulations, the deformation rate is kept constant at $\dot{u} = 10$ mm/min, while the moisture content varies from 0 to 3 wt%. Here, 3 wt% is considered as the saturation moisture content that can be contained in the polymer nanocomposites. The influence of moisture content on the material behavior of the nanocomposites is captured using the modified Guth–Gold model presented in Eq. (36). The simulation results show that the peak force, respectively, decreases from around 98 to 87 N and from $\tilde{5}0$ to 45 N at 296 and 346 K by increasing the moisture content from 1 to 2 wt%. The peak force, however, rises by further increasing the moisture to 3 wt%. For instance, the peak force increases from around 87 to 91 N at 296 K by increasing the moisture content from 2 to 3wt%. This observation can be interpreted as follows. The epoxy's moduli decrease

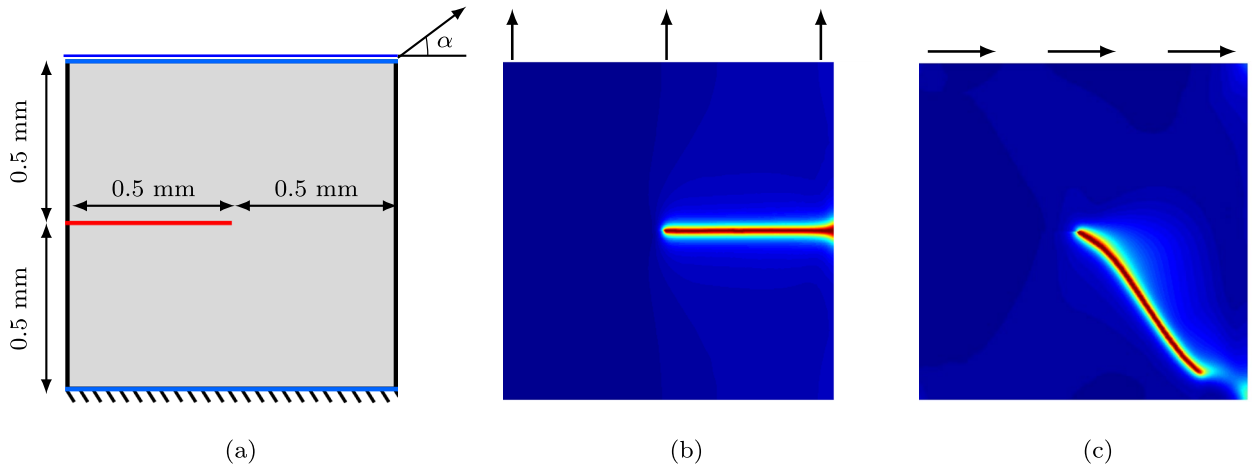

Fig. 10 **a** Geometry and boundary conditions of single-edge notched specimen, **b** fracture pattern for unidirectional tension ($\alpha = 90°$), and **c** fracture pattern for pure shear deformation ($\alpha = 0°$)

with moisture absorption when the moisture content is less than 1.7 wt%. However, when the moisture content exceeds 1.7 wt%, moduli regain some of their reduction as discussed in Eq. (36). Therefore, the peak force increases by increasing the moisture content from 2 to 3wt%.

Finally, the capability of the proposed model to predict fracture patterns is evaluated using the well-known single-edge notched tensile and shear tests of BNP(15 %wt)/epoxy samples. The geometry and boundary conditions are shown in Fig. 10a. A horizontal notch is placed at middle height from the left outer surface to the center of the specimen. The bottom side of the specimen is fixed, while the top side is moved. Both tensile and shear loads are applied at the deformation rate of $\dot{u} = 10$ mm/min with constant displacement increments of 10^{-4} mm. The simulations are performed at 296 K under plane strain conditions with the material parameters listed in Table 2. Meshes are refined in areas where cracks are expected to propagate. Accordingly, 12509 elements and an effective element size of 0.003 mm in the central strip of the specimen are generated for the tensile test, and 21045 elements with refined meshes in the lower right diagonal strip of the specimen are used for the shear test. Also, the length-scale parameter is set to be $l_0 = 0.015$ mm. The predicted fracture patterns for the two cases are shown in Figs. 10b, b. It can be seen that the crack path is horizontal for the tensile case, while there is a curved crack path for the pure shear case. The crack patterns are in agreement with those presented in the literature [43]. To study the effect of moisture on the fracture behavior of the nanocomposites, the tensile and shear tests are performed in both dry and wet

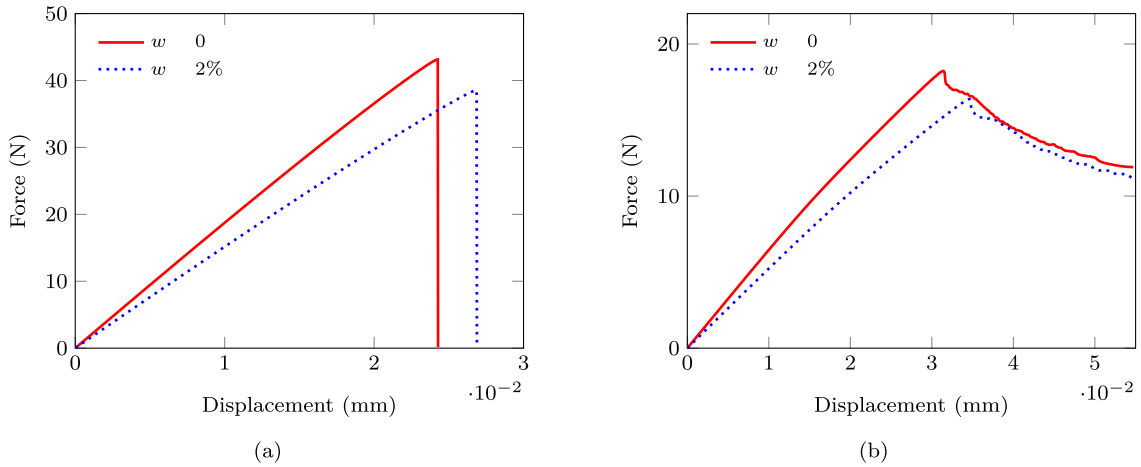

Fig. 11 Effect of moisture content on the force–displacement curve in single-edge notched simulation tests of BNP(15 %wt)/epoxy samples under **a** tensile and **b** shear loading

conditions. Figures 10a, b present the resulting force–displacement curves at the moisture content of 0 and 2 wt%. According to the simulation results, the peak force obtained from the tensile and shear tests, respectively, decreases from around 43 to 38 N and from 18 to 16 N by increasing the moisture content to 2 wt% (Fig. 11).

5 Summary and conclusion

A phase-field fracture model has been proposed to investigate the effect of hydrothermal effects on the fracture behavior of BNPs/epoxy nanocomposites at finite deformation. To explore the impact of nanoparticle and moisture contents on the rate-, temperature-dependent fracture evolution in the polymer nanocomposites, the PFM has been coupled to a nonlinear viscoelastic constitutive model in a thermodynamically consistent way. For this, the Helmholtz free energy, which describes the nanocomposites' rate, temperature, and moisture-dependent behavior, is additively decomposed into an equilibrium, a non-equilibrium, and a volumetric contribution with positive/negative components. Within this framework, modified versions of the Guth–Gold and Kitagawa models have been adopted to capture the role played by hydrothermal conditions on the fracture evolution in the materials. To improve the the computational efficiency of the PFM, a quasi-Newton monolithic algorithm proposed in [34, 64] has been employed to solve the coupled governing equations. The BFGS algorithm applied to nonlinear viscoelastic fracture problems confirms its higher efficiency in comparison with a staggered solution scheme. Benchmark examples show that recovering the monolithic solution using the staggered solution requires about ten times the cumulative number of iterations is about ten times more number of iterations.

To further evaluate the capability of the proposed PFM, numerical predictions should be compared with the experimental data at different hydrothermal conditions and strain rates in the future. Also, the effect of non-uniform dispersion of nanoparticles and moisture content and varying temperature profiles across a specimen on the fracture behavior of polymer nanocomposites needs to be investigated in future studies. Furthermore, interactions between water molecules, nanoparticles, and an epoxy matrix would cause changes in the material properties such as the viscosity and energy release rate. However, due to the complex interactions at small scales, the mechanisms leading to these possible variations are not clear. To gain a deep understanding of the microstructure's effect on the macroscopic properties, the phase-field modeling can be coupled to molecular models to characterize the polymer nanocomposites' material behavior [4, 5]. Furthermore, nanoparticles tend to form agglomerates in an epoxy matrix, resulting in insufficient dispersal [33]. It leads to degrading material properties due to relatively inferior interfacial interactions between nanoparticles and the matrix. The effect of surface modification of BNPs on the the fracture behavior of the polymer nanocomposites should be investigated in the future studies.

Acknowledgements This work originates from "Challenges of industrial application of nanomodified and hybrid material systems in lightweight rotor blade construction"("HANNAH - Herausforderungen der industriellen Anwendung von nanomodifizierten und hybriden Werkstoffsystemen im Rotorblattleichtbau") research project funded by the Federal Ministry for Economic Affairs and Energy. The authors wish to express their gratitude for the financial support. The authors also acknowledge the support of the LUIS scientific computing cluster, which is funded by Leibniz Universität Hannover, the Lower Saxony Ministry of Science and Culture (MWK), and the German Research Council (DFG).

Funding Open Access funding enabled and organized by Projekt DEAL.

Declarations

Conflict of interest The authors declare that they have no conflict of interest.

References

1. Ambati M, Kruse R, De Lorenzis L (2016) A phase-field model for ductile fracture at finite strains and its experimental verification. Computational Mechanics 57(1), 149–167
2. Amor H, Marigo JJ, Maurini C (2009) Regularized formulation of the variational brittle fracture with unilateral contact: Numerical experiments. Journal of the Mechanics and Physics of Solids 57(8), 1209–1229
3. Aranson I, Kalatsky V, Vinokur V (2000) Continuum field description of crack propagation. Phys Rev Lett 85(1):118
4. Arash B, Park HS, Rabczuk T (2015) Tensile fracture behavior of short carbon nanotube reinforced polymer composites: a coarse-grained model. Compos Struct 134:981–988
5. Arash B, Park HS, Rabczuk T (2016) Coarse-grained model of the j-integral of carbon nanotube reinforced polymer composites. Carbon 96:1084–1092
6. Arash B, Exner W, Rolfes R (2019) Viscoelastic damage behavior of fiber reinforced nanoparticle-filled epoxy nanocomposites:

multiscale modeling and experimental validation. Compos B Eng 174:107005
7. Arash B, Exner W, Rolfes R (2019) A viscoelastic damage model for nanoparticle/epoxy nanocomposites at finite strain: a multiscale approach. J Mech Phys Solids 128:162–180
8. Arash B, Unger R, Exner W, Rolfes R (2021) A finite deformation gradient-enhanced damage model for nanoparticle/polymer nanocomposites: an atomistically-informed multiscale approach. Compos Struct 258:113211
9. Bažant ZP (1991) Why continuum damage is nonlocal: micromechanics arguments. J Eng Mech 117(5):1070–1087
10. Bergström J, Boyce M (2000) Large strain time-dependent behavior of filled elastomers. Mech Mater 32(11):627–644
11. Bourdin B, Francfort GA, Marigo JJ (2000) Numerical experiments in revisited brittle fracture. Journal of the Mechanics and Physics of Solids 48(4), 797–826
12. Boyce M, Socrate S, Llana P (2000) Constitutive model for the finite deformation stress-strain behavior of poly (ethylene terephthalate) above the glass transition. Polymer 41(6), 2183–2201
13. Boyce MC, Weber G, Parks DM (1989) On the kinematics of finite strain plasticity. Journal of the Mechanics and Physics of Solids 37(5), 647–665
14. Brighenti R, Rabczuk T, Zhuang X (2021) Phase field approach for simulating failure of viscoelastic elastomers. Eur J Mech-A/Solids 85:104092
15. Chowdhury KA, Talreja R, Benzerga AA (2008) Effects of manufacturing-induced voids on local failure in polymer-based composites. ASME J Eng Mater Technol 130(2):021010. https://doi.org/10.1115/1.2841529
16. Cui T, Verberne P, Meguid S (2018) Characterization and atomistic modeling of the effect of water absorption on the mechanical properties of thermoset polymers. Acta Mechanica 229(2), 745–761
17. Dastgerdi JN, Anbarlooie B, Marzban S, Marquis G (2015) Mechanical and real microstructure behavior analysis of particulate-reinforced nanocomposite considering debonding damage based on cohesive finite element method. Composite Structures 122:518–525
18. Fan M, Jin Y, Wick T (2021) A quasi-monolithic phase-field description for mixed-mode fracture using predictor–corrector mesh adaptivity. Eng Comput. https://doi.org/10.1007/s00366-021-01423-6
19. Fang J, Wu C, Rabczuk T et al (2020) Phase field fracture in elasto-plastic solids: a length-scale insensitive model for quasi-brittle materials. Comput Mech 66:931–961
20. Fankhänel J, Arash B, Rolfes R (2019) Elastic interphase properties of nanoparticle/epoxy nanocomposites: a molecular dynamics study. Compos B Eng 176:107211
21. Francfort GA, Marigo JJ (1998) Revisiting brittle fracture as an energy minimization problem. Journal of the Mechanics and Physics of Solids 46(8), 1319–1342
22. Geers M, De Borst R, Brekelmans W, Peerlings R (1998) Strain-based transient-gradient damage model for failure analyses. Computer methods in applied mechanics and engineering 160(1–2):133–153
23. Gerasimov T, De Lorenzis L (2016) A line search assisted monolithic approach for phase-field computing of brittle fracture. Computer Methods in Applied Mechanics and Engineering 312:276–303
24. Germain P, Suquet P, Nguyen QS (1983) Continuum thermodynamics. ASME Transact Series E J Appl Mech 50:1010–1020
25. Goswami S, Anitescu C, Chakraborty S, Rabczuk T (2020a) Transfer learning enhanced physics informed neural network for phase-field modeling of fracture. Theoretical and Applied Fracture Mechanics 106:102447
26. Goswami S, Anitescu C, Rabczuk T (2020b) Adaptive fourth-order phase field analysis using deep energy minimization. Theoretical and Applied Fracture Mechanics 107:102527
27. Guth E (1945) Theory of filler reinforcement. Journal of applied physics 16(1):20–25
28. Heister T, Wheeler MF, Wick T (2015) A primal-dual active set method and predictor-corrector mesh adaptivity for computing fracture propagation using a phase-field approach. Computer Methods in Applied Mechanics and Engineering 290:466–495
29. Hesch C, Gil A, Ortigosa R, Dittmann M, Bilgen C, Betsch P, Franke M, Janz A, Weinberg K (2017) A framework for polyconvex large strain phase-field methods to fracture. Computer Methods in Applied Mechanics and Engineering 317:649–683
30. Hussein A, Kim B (2019) Micromechanics based fem study on the mechanical properties and damage of epoxy reinforced with graphene based nanoplatelets. Composite Structures 215:266–277
31. Jux M, Fankhänel J, Daum B, Mahrholz T, Sinapius M, Rolfes R (2018) Mechanical properties of epoxy/boehmite nanocomposites in dependency of mass fraction and surface modification-an experimental and numerical approach. Polymer 141:34–45
32. Kaya Z, Balcıoğlu HE, Gün H (2020) The effects of temperature and deformation rate on fracture behavior of S-2 glass/epoxy laminated composites. Polym Compos 41(11):4799–4810
33. Khorasani MGZ, Silbernagl D, Szymoniak P, Hodoroaba VD, Sturm H (2019) The effect of boehmite nanoparticles (γ-alooh) on nanomechanical and thermomechanical properties correlated to crosslinking density of epoxy. Polymer 164:174–182
34. Kristensen PK, Martínez-Pañeda E (2020) Phase field fracture modelling using quasi-newton methods and a new adaptive step scheme. Theoretical and Applied Fracture Mechanics 107:102446
35. Lee EH (1969) Elastic-plastic deformation at finite strains. J Appl Mech 36(1):1–6. https://doi.org/10.1115/1.3564580
36. Li Y, Tang S, Kröger M, Liu WK (2016a) Molecular simulation guided constitutive modeling on finite strain viscoelasticity of elastomers. Journal of the Mechanics and Physics of Solids 88:204–226
37. Li Y, Wang S, Arash B, Wang Q (2016b) A study on tribology of nitrile-butadiene rubber composites by incorporation of carbon nanotubes: molecular dynamics simulations. Carbon 100:145–150
38. Loew PJ, Peters B, Beex LA (2019) Rate-dependent phase-field damage modeling of rubber and its experimental parameter identification. Journal of the Mechanics and Physics of Solids 127:266–294
39. Matthies H, Strang G (1979) The solution of nonlinear finite element equations. International journal for numerical methods in engineering 14(11):1613–1626
40. May S, Vignollet J, de Borst R (2016) A new arc-length control method based on the rates of the internal and the dissipated energy. Eng Comput 33(1):100–115. https://doi.org/10.1108/EC-02-2015-0044
41. Miehe C (1996) Numerical computation of algorithmic (consistent) tangent moduli in large-strain computational inelasticity. Computer methods in applied mechanics and engineering 134(3–4):223–240
42. Miehe C, Mauthe S (2016) Phase field modeling of fracture in multi-physics problems. part iii. crack driving forces in hydro-poro-elasticity and hydraulic fracturing of fluid-saturated porous media. Computer Methods in Applied Mechanics and Engineering 304:619–655
43. Miehe C, Hofacker M, Welschinger F (2010) A phase field model for rate-independent crack propagation: robust algorithmic implementation based on operator splits. Comput Methods Appl Mech Eng 199(45–48):2765–2778
44. Miehe C, Welschinger F, Hofacker M (2010) Thermodynamically consistent phase-field models of fracture: variational principles

and multi-field fe implementations. Int J Numer Meth Eng 83(10):1273–1311
45. Msekh MA, Silani M, Jamshidian M, Areias P, Zhuang X, Zi G, He P, Rabczuk T (2016) Predictions of j integral and tensile strength of clay/epoxy nanocomposites material using phase field model. Composites Part B: Engineering 93:97–114
46. Msekh MA, Cuong N, Zi G, Areias P, Zhuang X, Rabczuk T (2018) Fracture properties prediction of clay/epoxy nanocomposites with interphase zones using a phase field model. Engineering Fracture Mechanics 188:287–299
47. Needleman A (1988) Material rate dependence and mesh sensitivity in localization problems. Computer methods in applied mechanics and engineering 67(1):69–85
48. Nguyen VD, Lani F, Pardoen T, Morelle X, Noels L (2016) A large strain hyperelastic viscoelastic-viscoplastic-damage constitutive model based on a multi-mechanism non-local damage continuum for amorphous glassy polymers. International Journal of Solids and Structures 96:192–216
49. N'guyen T, Lejeunes S, Eyheramendy D, Boukamel A (2016) A thermodynamical framework for the thermo-chemo-mechanical couplings in soft materials at finite strain. Mech Mater 95:158–171
50. Park H, Choi J, Kim B, Yang S, Shin H, Cho M (2018) Toward the constitutive modeling of epoxy matrix: temperature-accelerated quasi-static molecular simulations consistent with the experimental test. Compos B 142(1):131–141
51. Peerlings RH, de Borst R, Brekelmans WM, De Vree J (1996) Gradient enhanced damage for quasi-brittle materials. Int J Numer Meth Eng 39(19):3391–3403
52. Poh LH, Sun G (2017) Localizing gradient damage model with decreasing interactions. International Journal for Numerical Methods in Engineering 110(6), 503–522
53. Qi H, Boyce M (2005) Stress-strain behavior of thermoplastic polyurethanes. Mechanics of Materials 37(8), 817–839
54. Ren H, Zhuang X, Oterkus E, Zhu H, Rabczuk T (2021) Nonlocal strong forms of thin plate, gradient elasticity, magneto-electro-elasticity and phase field fracture by nonlocal operator method. arXiv preprint arXiv:2103.08696
55. Shen R, Waisman H, Guo L (2019) Fracture of viscoelastic solids modeled with a modified phase field method. Computer Methods in Applied Mechanics and Engineering 346:862–890
56. Singh N, Verhoosel C, De Borst R, Van Brummelen E (2016) A fracture-controlled path-following technique for phase-field modeling of brittle fracture. Finite Elements in Analysis and Design 113:14–29
57. Spitalsky Z, Tasis D, Papagelis K, Galiotis C (2010) Carbon nanotube-polymer composites: chemistry, processing, mechanical and electrical properties. Progress in polymer science 35(3):357–401
58. Sun W, Chaikof EL, Levenston ME (2008) Numerical approximation of tangent moduli for finite element implementations of nonlinear hyperelastic material models. ASME J Biomech Eng 130(6):061003. https://doi.org/10.1115/1.2979872
59. Unger R, Exner W, Arash B, Rolfes R (2019) Non-linear viscoelasticity of epoxy resins: molecular simulation-based prediction and experimental validation. Polymer 180:121722
60. Unger R, Arash B, Exner W, Rolfes R (2020) Effect of temperature on the viscoelastic damage behaviour of nanoparticle/epoxy nanocomposites: constitutive modelling and experimental validation. Polymer 191:122265
61. Vandoren B, Simone A (2018) Modeling and simulation of quasi-brittle failure with continuous anisotropic stress-based gradient-enhanced damage models. Computer Methods in Applied Mechanics and Engineering 332:644–685
62. Ward IM, Sweeney J (2012) Mechanical properties of solid polymers. John Wiley & Sons, Hoboken
63. Wu JY (2017) A unified phase-field theory for the mechanics of damage and quasi-brittle failure. Journal of the Mechanics and Physics of Solids 103:72–99
64. Wu JY, Huang Y, Nguyen VP (2020) On the BFGS monolithic algorithm for the unified phase field damage theory. Computer Methods in Applied Mechanics and Engineering 360:112704
65. Yin B, Kaliske M (2020) Fracture simulation of viscoelastic polymers by the phase-field method. Computational Mechanics 65(2), 293–309
66. Zhou J, Lucas JP (1999) Hygrothermal effects of epoxy resin. Part i: the nature of water in epoxy. Polymer 40(20):5505–5512
67. Zhou S, Zhuang X, Zhu H, Rabczuk T (2018) Phase field modelling of crack propagation, branching and coalescence in rocks. Theoret Appl Fract Mech 96:174–192